2024 IEEE International Conference on Robotics and Automation (ICRA 2024)
May 13-17, 2024. Yokohama, Japan

Remote Control of Untethered Magnetic Robots within a Lumen using X-Ray-Guided Robotic Platform

Leendert-Jan W. Ligtenberg[1], Nicole C. A. Rabou[1], Sander Peters[1,2]
Trishal Vengetela[1], Vincent Schut[2], H. Remco Liefers[3], Michiel Warlé[4] and Islam S. M. Khalil[1,3]

***Abstract*— Until now, the potential of untethered magnetic robots (UMRs), propelled by external time-periodic magnetic fields, has been hindered by the limitations of wireless manipulation systems or noninvasive imaging techniques combined. The need for simultaneous actuation and noninvasive localization imposes a strict constraint on both functionalities. This study addresses this challenge by substantiating the feasibility through experimental validation, showcasing the direct teleoperation of UMRs within a fluid-filled lumen. This teleoperation capability is facilitated by a scalable X-ray-guided robotic platform, extendable to match the dimensions required for *in vivo* applications, marking a noteworthy advancement. Our methodology is demonstrated by teleoperating a 12-mm-long screw-shaped UMR (5 mm in diameter) within a bifurcated lumen, filled with blood. This navigation is achieved using controlled rotating magnetic fields, guided by real-time X-ray Fluoroscopy images. Incorporating a two-degree-of-freedom control system, we demonstrate the operator's capability to use X-ray Fluoroscopy images to keep the UMR coupled with the external field during wireless teleoperations, resulting in a success rate of 76.6% when moving along the intended pathways, with a mean absolute position error of 1.6 ± 2.1 mm.**

I. INTRODUCTION

Achieving efficient manipulation of untethered magnetic robots (UMRs) within bodily fluids and tissues has been successfully accomplished by utilizing external stimuli, primarily magnetic fields [1], [2]. These external stimuli provide the essential power required for locomotion and precise directional control over a distance, thus enabling innovative diagnostic and therapeutic procedures that were previously unattainable. As more locations within the human body become accessible, this approach unlocks unprecedented possibilities. However, navigating controllably within these natural pathways demands feedback control to guide the UMR along the intended trajectory.

Implementing this feedback control through teleoperation offers convenience by giving clinicians complete control over the UMR during potential interventions, and this requirement is driven by two fundamental reasons. First, accurately modeling the motion dynamics of the UMR for calculating model-based control inputs (physical-model-based approach) might prove challenging. Second, it is inherently safer for the user to conduct the intervention without decreasing the clinician's authority over control. Satisfying this requirement mandates the integration of an imaging system and a wireless manipulation system. These components empower clinicians to base their inputs on real-time medical images, delivering comprehensive insights into the UMR's position and orientation, physical surroundings, and intended path [3].

Recently, there has been rapid progress in integrating noninvasive imaging systems (such as computed tomography [4], magnetic resonance [5], ultrasound [6], photoacoustic imaging [7], electrical impedance tomography [8], magnetic localization [9], X-ray visualization [10], and X-ray guided teleoperation of a guidewire [11]) with magnetic manipulation systems. This integration has facilitated the implementation of wireless actuation and motion control experiments under conditions similar to those encountered *in vivo*, or even the achievement of wireless control directly within *in vivo* environments [12], [13]. In these methods, opting for teleoperation of the UMR without the need for a physical model might offers greater advantage. By coupling the UMR with external stimuli through a teleoperation system, operators can effectively guide its movement along the intended trajectory. In this case, the physical model of the UMR would be used offline to create a useful mapping between its inputs and motion dynamics. Once equipped with this mapping, the control inputs can be predicted based on the physical conditions of the surroundings and the UMR (e.g., vessel diameter, blood flow, viscosity, and step-out).

In this study, we develop an interventional X-ray-guided robotic platform for the direct teleoperation of UMRs (screw-type). The control inputs, including actuation frequency, field strength, and the rotation axis of the rotating field, are determined based on the intended trajectory and anticipated response of the UMR. These inputs serve as the foundation for a 2-degree-of-freedom (DOF) control system. This system operates by calculating the joint-space coordinates of the wireless manipulation system from X-ray Fluoroscopy images of the environment collected offline. Then, we dynamically modulate the swimming speed of the UMR by adjusting the actuation frequency via teleoperation, which is guided by real-time positional data visualized through X-ray Fluoroscopy images. This process ensures precise alignment between the actuator magnet and the UMR. The rest of the paper is structured as follows: Section II offers insights into the robotic platform (Fig. 1) and technical integration details of its core components, namely the C-Arm imaging

[1]The authors are with the Department of Biomechanical Engineering, University of Twente, 7500 AE Enschede, The Netherlands.
[2]The authors are with the Saxion University of Applied Sciences, 7513 AB Enschede, The Netherlands.
[3]The authors are with the Technical Medical Centre, University of Twente, 7500 AE Enschede, The Netherlands.
[4]M. Warlé is with Radboud University Medical Center, 6525 GA Nijmegen, The Netherlands.
This work was supported by the Twente University RadBoudumc Opportunities (TURBO) program 2022 and Grant Crazy-Research-2022.

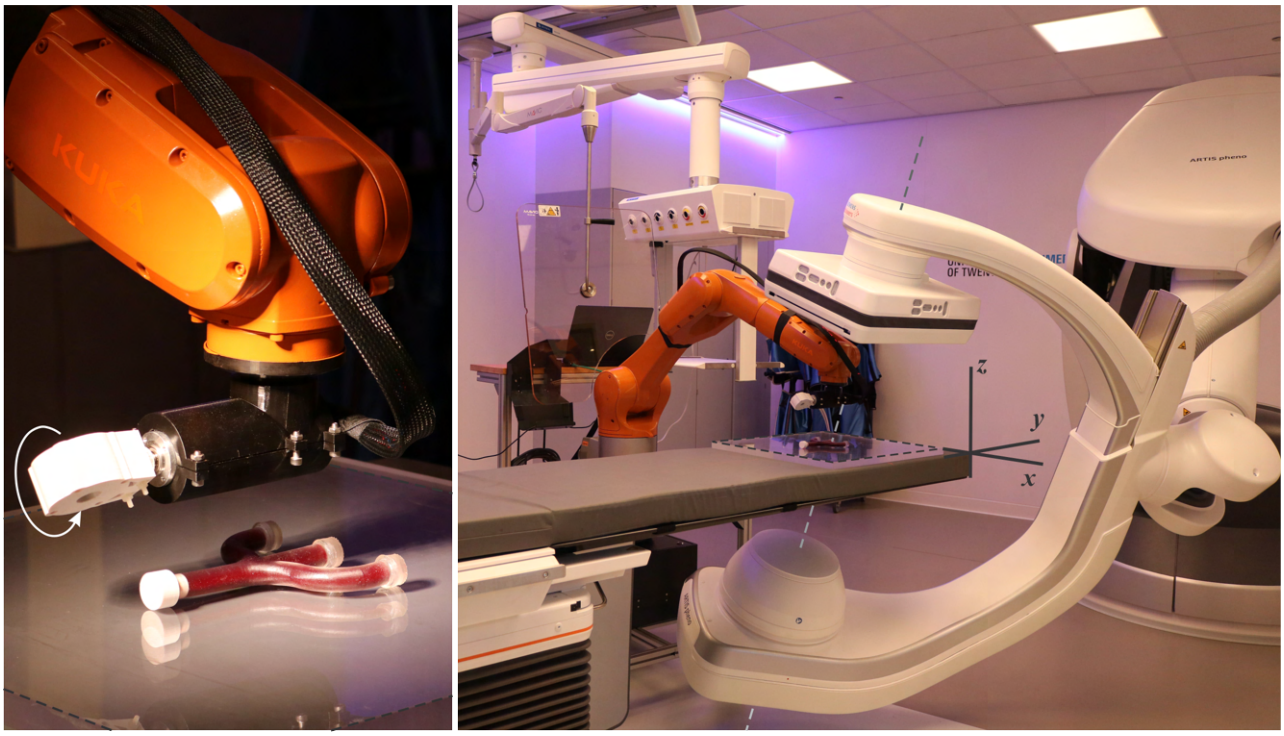

Fig. 1. The robotic platform consists of two key components: a C-ARM imaging system and a wireless manipulation system. These components work in tandem to achieve precise localization and wireless actuation. The UMR is contained within a fluid-filled lumen and guided using rotating magnetic fields.

system and wireless manipulation system. Our teleoperation control strategy is outlined in Section III, where we focus on the motion dynamics of the UMR within a confinement and the development of a 2-DOF control configuration. The validation of our teleoperation strategy and robotic platform is presented in Section IV, using scenarios involving curved and bifurcated fluid-filled lumens. Finally, Section V provides conclusions and outlines directions for future research.

II. INTERVENTIONAL X-RAY-GUIDED ROBOTIC PLATFORM

The X-Ray-Guided robotic platform is illustrated in Fig. 1. The X-ray source and detector (Siemens Healthineers Artis Pheno, Erlangen, Germany) possess three rotational degrees of freedom and one translational degree of freedom. While these three degrees of freedom would enable us to reconstruct any environment, we constrain the configuration to achieve real-time feedback essential for teleoperation at appropriate frame rates. The X-ray source-detector axis (dashed gray line) is fixed at an angle of 20° relative to the $\boldsymbol{z}$-axis (in the frame of reference in Fig. 1). This configuration enables us to reconstruct the environment of any curved or bifurcated lumen, and the translational degree of freedom can be utilized to minimize geometric blur. Acceptable signal-to-noise ratio is obtained using clinical radiation level with a fluoroscopy dose rate of 0.13 mGy.cm^{2}s^{-1}, as shown in Fig. 2. Additionally, with this oblique configuration, we create a relatively large workspace, granting the end-effector of a robotic manipulator greater access over the lumen.

The robotic manipulator (KUKA KR-10 1100-2, KUKA, Augsburg, Germany) is employed to control the positioning of a rotating permanent magnet (RPM) actuator [15], generating a magnetic field of about 5 mT at a gap of 7 cm that undergoes rotation within the operational area of the lumen. With 6-DOF, the robotic manipulator adeptly manages the RPM's rotation axis, thereby achieving precise control over the magnetic field's orientation exactly at the UMR's location within the lumen. When considering a UMR endowed with a magnetic moment perpendicular to its longitudinal axis, introducing a rotating magnetic field revolving around the $\boldsymbol{y}$-axis enables propulsion along the lumen, as demonstrated in Fig. 2. To accomplish forward and backward straight movements within the lumen, the robotic manipulation of the RPM's rotation axis aligned with the $\boldsymbol{y}$-axis is essential. Moreover, if desired, the manipulation of the RPM's rotation axis about the $\boldsymbol{z}$-axis facilitates the exertion of in-plane torque to steer the UMR. Similarly, the RPM's rotation axis can be controlled about the $\boldsymbol{x}$-axis to steer the UMR out-of-plane with a non-zero pitch angle.

The operator has the capability to manipulate the RPM-actuator's position from a protected area behind a radiation shield during experimental sessions. The C-Arm's oblique setup delivers real-time X-ray Fluoroscopy images encompassing the RPM-actuator, the UMRs, and the contours of the curved lumen. As depicted in Fig. 2, the radiopaque objects stand out distinctly, facilitating the straightforward identification of both the RPM's and UMR's rotation axes. The RPM is composed of a cylindrical permanent magnet (with magnetic moment $\mathbf{M}$) rigidly affixed to a DC motor. Notably, the magnetic moment of this permanent magnet aligns

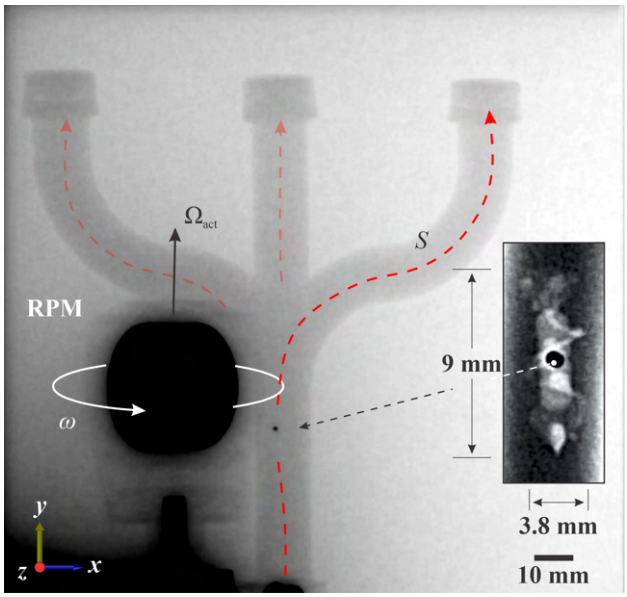

Fig. 2. An X-ray Fluoroscopy image captures a UMR navigating within a curved lumen. The curvature of the lumen is defined by the tangent angle ($\psi(S)$) relative to the arc length S. The UMR's movement involves a dual action: rotation of the RPM around the rotation axis $\mathbf{\Omega}_{\text{act}}$ and controlled steering facilitated by in-plane torque applied about the $\boldsymbol{z}$-axis. The inset shows the UMR visualized through the utilization of a radiocontrast agent.

perpendicularly to the rotation axis $\mathbf{\Omega}_{\text{act}}$. This orientation allows for the alignment of the RPM's rotation axis with the curved lumen's centerline based on the X-ray Fluoroscopy images. Similarly, the UMR features a non-magnetic screw-shaped body housing a 1 mm cylindrical permanent magnet. This magnet intercepts radiation, precluding the passage of X-rays. Consequently, it is feasible to determine the position of the permanent magnet while the UMR's geometric details remain undisclosed through X-ray imaging.

III. TELEOPERATION CONTROL STRATEGY

Our UMR is a screw-type, featuring a non-magnetic screw-shaped body complemented by a rigidly attached permanent magnet. This configuration incorporates a helical wave pattern onto a cylinder. The magnet enables versatile motion capabilities, including rotation along the longitudinal axis for propulsion, as well as in-plane and out-of-plane rotations essential for executing yawing and pitching maneuvers, respectively. This level of control is accomplished by a rotating magnetic field generated by position-controlled RPM-actuator. This control system is composed of two parts: The first involves a predictive feedforward control input, $\mathcal{F}$. Computed based on the contours of the surrounding blood vessels, regardless of their diverse morphologies, this input enables the UMR to autonomously adjust its orientation to the ever-changing vessel geometries. The second is the X-Ray-Guided control input $\mathcal{C}$, an operator intervention. This input takes into account the hard-to-model dynamics, giving the operator real-time control rooted in X-ray feedback, I. Combining these two inputs allows for the simultaneous control of the RPM's rotation axis and its rotational speed, ω. This integration is what generates the targeted rotating magnetic field, $\mathbf{B}$, and the intended torque on the UMR (Fig. 3).

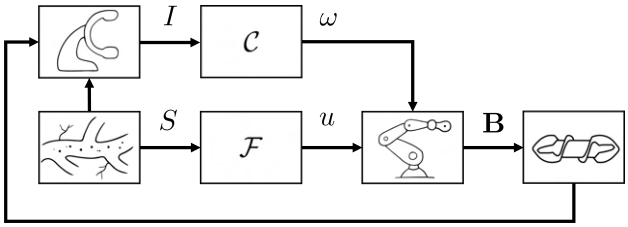

Fig. 3. The 2-DOF control configuration for an untethered magnetic robot (UMR) within a vascular model utilizes predefined confinement geometry and real-time UMR positioning through X-ray imaging. The control system $\mathcal{F}$ determines the joint-space coordinates u of the robotic manipulators over time based on the centerline of the curved lumen and expected UMR translational velocity, while the control system $\mathcal{C}$ is calculated based on the position of the UMR with respect to the RPM.

A. Predictive Feedforward Control Input $\mathcal{F}$

Considering a curved lumen with an arbitrary shape, it is possible to approximate any small segment of its boundary using a continuous curve function. Once this continuous function is derived from the known digital points within the field of view (Fig. 2), we can accurately ascertain both the tangent angle and curvature at any point of interest along the curve. If the curve is described by the parametric equation $\{x(S), y(S)\}$, where S is the arc length, then the slope of the tangent line, $m(S)$, at any point is given by

$$m(S) = \frac{\mathrm{d}y/\mathrm{d}S}{\mathrm{d}x/\mathrm{d}S}, \quad \text{and} \quad \psi(S) = \tan^{-1} m(S), \tag{1}$$

where $\psi(S)$ represents the tangent angle at a specific point. Through the derivative of $\psi(S)$ with respect to the arc length, we acquire the instantaneous rate of change, curvature. This curvature can be expressed as follows:

$$\mathcal{K}(S) = \frac{\mathrm{d}\psi(S)}{\mathrm{d}S}. \tag{2}$$

Utilizing the local tangent, we can determine the intended rotation axis of the RPM, $\mathbf{\Omega}_{\text{act}}$. Concurrently, the curvature will provide insight into the geometric attributes at the designated point of interest. If the rotation axis and position of the RPM are constrained in a manner where the field rotation axis in the vicinity of the UMR aligns parallel to the local tangent, it becomes feasible to calculate the desired joint-space variables of the 6-DOF robotic manipulator.

The configuration-to-pose kinematics of the robotic manipulator, denoted as $\{\mathbf{p}_{\text{act}}, \mathbf{R}\} = \mathcal{L}(\boldsymbol{q})$, enables precise control over the RPM-actuator's pose. Therefore, for a given desired field rotation axis we can determine the joint-space coordinates, $\boldsymbol{q}$ using the position of the UMR within the curved lumen. We use the following velocity-level kinematics to compute the joint-space variables [14], [15]:

$$\begin{pmatrix} \dot{\mathbf{p}}_{\text{act}} \\ \dot{\mathbb{M}} \end{pmatrix} = \begin{pmatrix} \mathbb{I} & 0 \\ 0 & \mathrm{SK}(\mathbb{M})^{\mathrm{T}} \end{pmatrix} \mathbf{J}_{\mathrm{m}}(\boldsymbol{q})\dot{\boldsymbol{q}} = \mathbf{J}_{\mathrm{A}}(\boldsymbol{q})\dot{\boldsymbol{q}}, \tag{3}$$

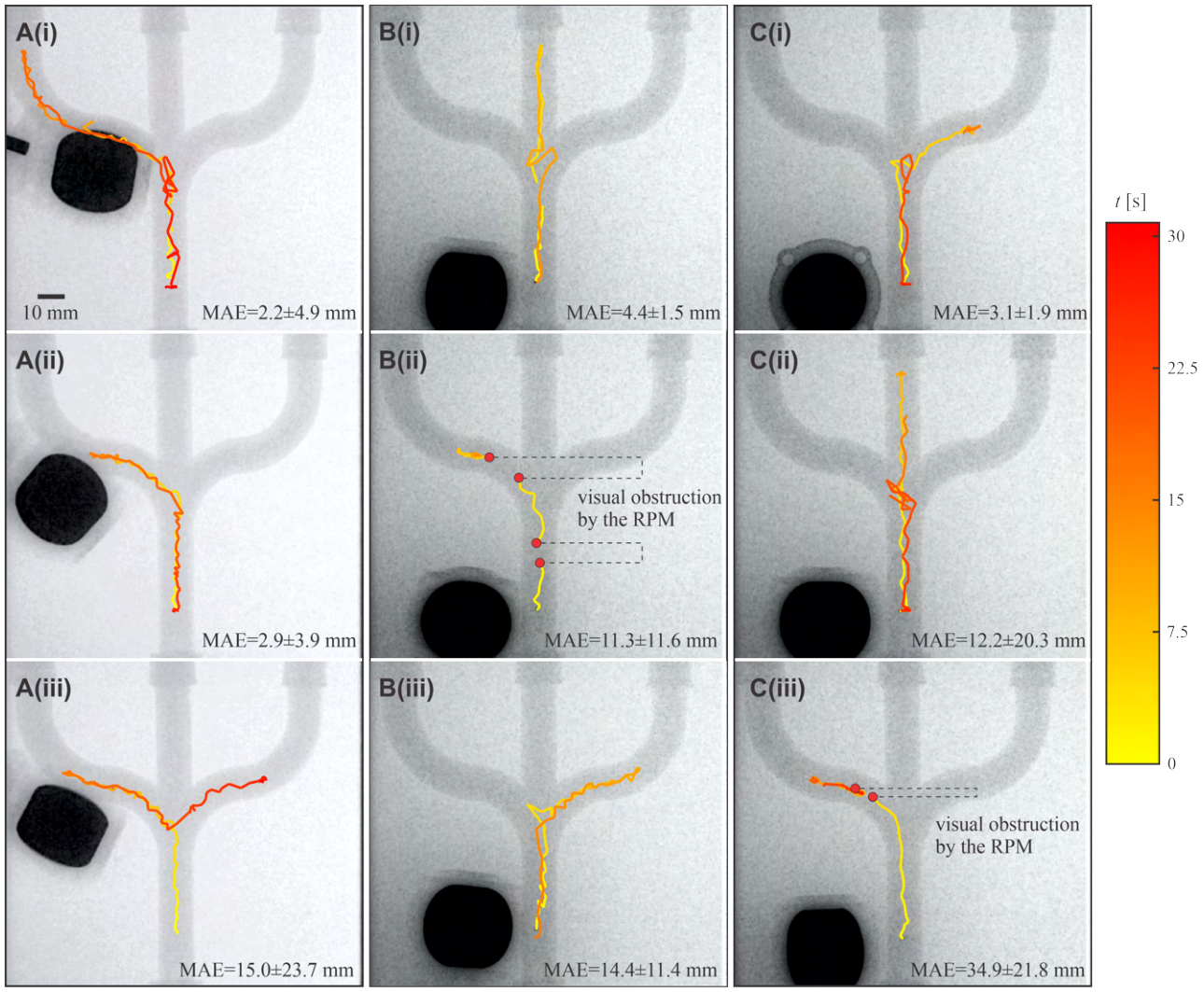

Fig. 4. Control of the UMR is implemented through the control system $\mathcal{F}$, which relies on the geometry of the desired path and the UMR speed. The success rate is assessed by conducting 10 trials along the left, straight, and right lumens. The UMR is controlled to move forward toward the distal end of any of the paths and subsequently return to the starting point. The mean absolute position error (MAE) is calculated using 10 trials. (A) The UMR achieves a success rate of 90% in the left lumen. (B) In the straight lumen, the success rate is 60%. (C)) The UMR's success rate in the right lumen is 20%. Please refer to supplementary multimedia.

where $\mathrm{SK}(\cdot)$ is the skew-symmetric operator of the cross product, $\mathbf{J}_{\mathrm{m}}$ is the geometric Jacobian, and $\mathbf{J}_{\mathrm{A}}$ is the RPM-actuator Jacobian. Taking into account the swimming speed of the UMR and the gradient of the tangent line at the UMR's location, Equation (3) can be applied to compute the joint-space variables, $\boldsymbol{q}$.

B. X-Ray-Guided Control Input $\mathcal{C}$

The open-loop nature of control system, $\mathcal{F}$, depends on the UMR's ability to maintain the magnetic coupling with the RPM by moving along at the same speed. In real-world scenarios, the swimming speed of the UMR will be influenced by various factors, including the wall effect, blood flow dynamics, and other hard-to-model behaviors. Therefore, feedback control, $\mathcal{C}$, is provided by the operator to compensate for any undesirable response during actuation.

Our feedback control is constrained to modifying the swimming speed solely by manipulating the actuation frequency of the RPM. For instance, if the UMR's movement deviates from the RPM actuator's predictions according to physical-models, the operator can directly fine-tune the actuation frequency to uphold the intended magnetic coupling. This adjustment is performed directly using the collected X-ray Fluoroscopy images. The speed of the UMR scales linearly with the actuation frequency for a given fluid and geometry. This linear correlation remains valid below a step-out frequency, determined by the magnetic and drag torque applied to the UMR.

Note that the control law $\mathcal{F}$ is fully capable of maneuvering the UMR within any curved lumen. Nevertheless, the feedback input, $\mathcal{C}$, provided by the operator is expected to enhance control accuracy by improving the magnetic coupling between the UMR and the RPM actuator, and by controlling the UMR's swimming speed at the bifurcation. This hypothesis could be confirmed through a comparative

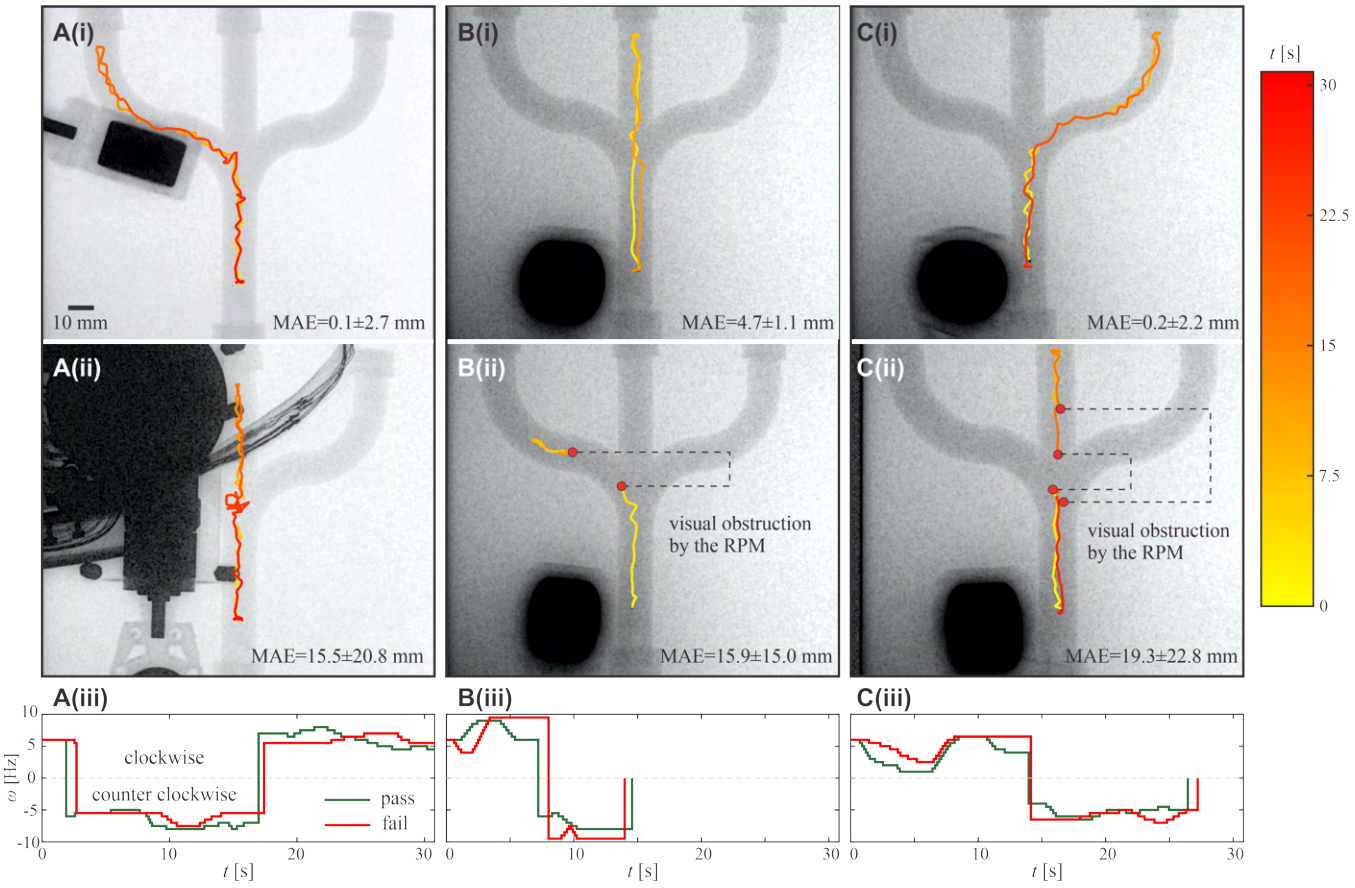

Fig. 5. Control of the UMR is implemented through the $\mathcal{F}$+$\mathcal{C}$ control system, which relies on the geometry of the desired path and the UMR speed. The success rate is assessed by conducting 10 trials along the left and right lumens, as well as the straight lumen. In each trial, the UMR is controlled to move forward toward the distal end of any of the paths and subsequently return to the starting point. (A) The UMR achieves a success rate of 90% in the left lumen. (B) In the straight lumen, the success rate is 60%. (C) The UMR's success rate in the right lumen is 80%. Please refer to supplementary multimedia.

experimental study, assessing the success rate of UMR movement within blood-filled curved lumens.

IV. EXPERIMENTAL RESULTS

A. Experimental Setup

We conduct motion control experiments with the UMR inside a 3D-printed vessel phantom. The UMR has a length of 9 mm and outer diameter 3.8 mm with an affixed NdBFe Grade-N45 permanent magnet, 1 mm in diameter and height. The resulting step-out frequency of such UMR in blood is 28 Hz with a velocity of 34 mm/s, the UMR is coated with LipoCoat 4AC coating technology to ensure hemocompatibility. The phantom exhibits a pitchfork configuration, facilitating the evaluation of control characteristics within three distinct pathways. Each pathway has an inner diameter of 9.5 mm. The phantom is filled with heparinized porcine blood, and the long axis of the straight pathway aligns with the y-axis in the frame of reference illustrated in Fig. 1. In each control trial, the UMR is precisely controlled, with an actuation frequency of 9 Hz, to swim from the proximal end of the phantom to the distal end of one of the pathways and then return. The success of each trial is determined by the control system's ability to maneuver the UMR controllably along the intended pathway and bring it back to the starting point. The mean absolute position error (MAE) is determined in each trial by assessing the deviation of the UMR from the centerline of the intended pathway. Two control configurations are evaluated: the first utilizes the predictive feedforward input $\mathcal{F}$, while the second is the 2-DOF control configuration $\mathcal{F}+\mathcal{C}$. In control system $\mathcal{F}$, both the UMR and the wireless manipulation system operate autonomously, with no direct operator involvement. In control system $\mathcal{F}$+$\mathcal{C}$, the operator offers limited corrections to the swimming speed, while the motion of the robotic arm is automatically determined based on the configuration of each pathway.

B. Controlled Actuation with the $\mathcal{F}$ Controller

Fig. 4 illustrates motion control trials of the UMR using control system $\mathcal{F}$. For each pathway, we conduct 10 control trials, each comprising two consecutive runs: one from the proximal end of the phantom to the distal end of the path, and the other returning to the starting point. When the UMR is controlled along the left curved lumen (Fig. 4A), we achieve a success rate of 90%. Figs. 4A(i) and A(ii) provide two successful trials with MAE of 2.2 ± 4.9 and 2.9 ± 3.9 mm, respectively. Notably, in this pathway, backward motion proves to be more challenging due to the UMR's rotational direction, which induces a sideway drift opposing the in-plane torque

used for steering. Consequently, as demonstrated in the trial in Fig. 4A(iii), the UMR incorrectly enters the unintended path into the right curved lumen.

When the UMR is assigned the task of moving along the straight path, the success rate of the control system drops to 60%, as shown in Fig. 4B. A successful trial of the UMR along the straight pathway is achieved with a MAE of 4.4 ± 1.5 mm (Fig. 4B(i)). It is worth noting that the UMR's path inside the left curved lumen is obscured temporarily by the RPM itself, resulting in a disconnected appearance in the X-ray Fluoroscopy image (Fig. 4B(ii)). In the trial depicted in Fig. 4B, the UMR enters another unintended pathway, specifically the right curved lumen.

Finally, when the control system $\mathcal{F}$ is adjusted to guide the UMR along the right curved lumen, the success rate decreases to 20%. Fig. 4C illustrates three distinct trials in which the UMR is directed to swim along the right curved lumen. Some trials successfully follow the intended path (Fig. 4C(i)). However, executing in-plane rotations by rotating the RPM's rotation axis clockwise has presented challenges. When the UMR is actuated to rotate about its long axis while moving forward, it tends to drift sideways (Figs. 4C(ii) and 4C(iii)), influenced by the direction of rotation. This behavior becomes particularly evident when the UMR is actuated far from any solid boundary. In such cases, it is expected that the UMR will follow a curved trajectory as it moves forward [1]. Hence, executing a turning maneuver (clockwise rotation about the z-axis) proved to be more challenging for the UMR, primarily due to the sideways drift induced by the screwing motion, which counteracted the in-plane torque required for steering. In such situations, the operator can offer additional input to enhance steering.

C. Controlled Actuation with the $\mathcal{F} + \mathcal{C}$ Controller

The previous control maneuvers are replicated using the control system $\mathcal{F} + \mathcal{C}$, allowing the operator to regulate the UMR's swimming speed based on its position in the X-ray Fluoroscopy images (Fig. 5). In the left curved lumen, the success rate of the $\mathcal{F} + \mathcal{C}$ configuration remains at 90% (Fig. 5A). Regardless of the control configuration, the UMR can easily access this path because the sideway drift caused by screwing and the in-plane steering torque (counterclockwise about the z-axis) act in the same direction (Fig. 5A(i)). Note that the difference between the control inputs provided by the operators in the successful and failed trials is quite similar. Fig. 5A(ii) displays the UMR's response when the operators adjusted its angular velocity based on visual feedback. Despite the similarities in the control inputs shown in Fig. 5A(iii), the UMR's responses vary significantly. Therefore, it is crucial to enhance the steering torque at the location of the bifurcation.

Similar to the $\mathcal{F}$ controller, when the $\mathcal{F} + \mathcal{C}$ controller is employed to guide the UMR along the straight lumen, the success rate is measured at 60% (e.g., Fig. 5B(i)). Notably, in all unsuccessful trials (e.g., Fig. 5B(ii)), the UMR entered the left curved lumen. Fig. 5B(iii) illustrates the two inputs associated with both successful and failed trials, underscoring the significance of the control action at the bifurcation point, where the UMR could potentially enter an unintended pathway. A significant improvement in the success rate is observed for the right lumen, where a success rate of 80% is measured (Fig. 5C). Here the UMR's actuation frequency was decreased to ensure strong magnetic steering torque throughout the turn into the right lumen. This demonstrates the significance of the operator's input through the control system $\mathcal{C}$.

The integration of real-time X-ray Fluoroscopy imaging with RPM control allows operators to visually guide the UMR through complex vascular pathways, making it a promising technique for medical applications where precise navigation is crucial. We observe the importance of operator involvement in UMR control, especially in challenging scenarios. The operator's ability to adjust the UMR's movements based on the visual feedback from X-ray Fluoroscopy significantly improved success rates. This finding suggests that while automation is valuable, operator input remains critical, particularly in intricate tasks.

Our study also uncovers challenges in executing in-plane rotations. Sideways drift induced by the UMR's screwing motion posed difficulties in these maneuvers. This observation informs future research directions, encouraging the development of more robust control strategies to address such challenges. Nevertheless, our work showcases the potential of combining real-time imaging with UMR control for medical applications. It emphasizes the complementary role of operators in controlling UMRs and highlights challenges that can guide future research in this field.

V. CONCLUSIONS

This study highlights the effectiveness of a predictive feedforward control system ($\mathcal{F}$) and a 2-DOF control system ($\mathcal{F} + \mathcal{C}$) in guiding a UMR through complex vascular pathways using an X-ray-guided robotic platform. Control system $\mathcal{F}$ demonstrated successful tracking in the left curved lumen but faced challenges in the straight lumen and the right curved lumen. The addition of operator control in $\mathcal{C}$ significantly improved success rates, especially in the right curved lumen. However, the study revealed challenges in executing in-plane rotations, particularly clockwise rotations about the z-axis, due to the counteracting effects of the UMR's screwing motion-induced sideways drift. This underscores the importance of operator involvement in controlling screw-type UMRs in complex environments and suggests future research directions to refine control algorithms, increase autonomy, and explore different UMR designs and actuation methods to overcome these challenges while improving navigation.

ACKNOWLEDGEMENTS

The authors would like to thank Jeffrey R. Nagel for his invaluable assistance in fabricating the pitchfork phantom, Dr. Doronthee Wasserberg and Dr. Emily A.M. Klein Rot for their contributions to coating the swimmers, and Iris Mulder for her work on the illustrations in Fig. 3.

REFERENCES

[1] N. D. Nelson, J. Delacenserie and J. J. Abbott, "An empirical study of the role of magnetic, geometric, and tissue properties on the turning radius of magnetically driven screws," in *Proceedings of the IEEE International Conference on Robotics and Automation (ICRA)*, Karlsruhe, Germany, pp. 5372-5377, 2013.

[2] J. Leclerc, H. Zhao, D. Bao, and A. T. Becker, "In Vitro design investigation of a rotating helical magnetic swimmer for combined 3-D navigation and blood clot removal," *IEEE Trans. Robot.*, vol. 36, no. 3, pp.975-982, 2020.

[3] A. Aziz, S. Pane, V. Iacovacci, N. Koukourakis, J. Czarske, A. Menciassi, M. M. Sánchez, and O. G. Schmidt, "Medical imaging of microrobots: Toward in vivo applications," *ACS Nano*, vol. 14, no. 9, pp. 10865-10893, Sep. 2020.

[4] A. Hong, A. J. Petruska and B. J. Nelson, "Tracking a magnetically guided catheter with a single rotating C-Arm," in *Proceedings of the IEEE International Conference on Robotics and Automation (ICRA)*, Seattle, WA, pp. 618–623, 2015.

[5] J. B. Mathieu, G. Beaudoin, and S. Martel, "Method of propulsion of a ferromagnetic core in the cardiovascular system through magnetic gradients generated by an MRI System," *IEEE Trans. Biomed. Eng.*, vol. 53, pp. 29–299, 2006.

[6] Q. Wang, L. Yang, J. Yu, P. W. Y. Chiu, Y.-P. Zheng, and L. Zhang, "Real-Time magnetic navigation of a rotating colloidal microswarm under ultrasound guidance," *IEEE Trans Biomed Eng.*, vol. 67, no. 12, Dec. 2020.

[7] L. V. Wang, J. Yao. A practical guide to photoacoustic tomography in the life sciences. *Nat. Methods*, 13, 627(2016).

[8] H. Daguerre, S. O. Demir, U. Culha, F. Marionnet, M. Gauthier, M. Sitti, and A. Bolopion, "A localization method for untethered small-scale robots using electrical impedance tomography," *IEEE/ASME Transactions on Mechatronics*, vol. 27, no. 5, pp. 3506-3516, Oct. 2022.

[9] F. Bianchi, A. Masaracchia, E. S. Barjuei, A. Menciassi, A. Arezzo, A. Koulaouzidis, D. Stoyanov, P. Dario, and G. Ciuti, "Localization strategies for robotic endoscopic capsules: a review," *Expert Review of Medical Devices*, vol. 16, no. 5, pp. 381-403, May 2019.

[10] Wang, T., Ugurlu, H., Yan, Y. et al. "Adaptive wireless millirobotic locomotion into distal vasculature." *Nat Commun*, vol. 13, 4465(2022).

[11] Y. Kim, E. Genevriere, P. Harker, J. Choe, M. Balicki, R. W. Regenhardt, J. E. Vranic, A. A. Dmytriw, A. B. Patel, X. Zhao, "Telerobotic neurovascular interventions with magnetic manipulation." *Science Robotics*, vol. 7, no. 65, April 2022: eabg9907.

[12] A. Servant, F. Qiu, M. Mazza, K. Kostarelos, B. J. Nelson, "Controlled in vivo swimming of a swarm of bacteria-like microrobotic flagella," *Advanced Materials*, vol. 27, no. 19, pp. 2981-2988, Apr. 2015.

[13] E. E. Niedert, C. Bi, G. Adam, E. Lambert, L. Solorio, C. J. Goergen, and D. J. Cappelleri, "A tumbling magnetic microrobot system for biomedical applications," *Micromachines*, vol. 11, no. 9, Sep. 2020.

[14] R. Venezian and I. S. M. Khalil, "Understanding robustness of magnetically driven helical propulsion in viscous fluids using sensitivity analysis," *Advanced Theory and Simulations*, vol. 5, p. 2100519, 2022.

[15] T. W. R. Fountain, Prem V. Kailat, and J. J. Abbott, "Wireless control of magnetic helical microrobots using a rotating-permanent-magnet manipulator," in *Proc. IEEE Int. Conf. Robot. Autom.*, 2011, pp. 576–581.